Materials Transactions, Vol. 64, No. 7 (2023) pp. 1284 to 1298
Special Issue on Superfunctional Nanomaterials by Severe Plastic Deformation

Nanostructuring of Multi-Principal Element Alloys by Severe Plastic Deformation: from Fundamentals to an Improved Functionality

Jenő Gubicza* and Pham Tran Hung

Department of Materials Physics, Eötvös Loránd University, Budapest, Pázmány Péter sétány 1/A., H-1117, Hungary

Multi-principal element alloys (MPEAs) are in the forefront of materials science since their compositions can be found in the undiscovered central parts of phase diagrams. These materials contain 3–6 elements with similar fractions, i.e., the constituents do not play the classical solvent and solute roles in the alloys. This class of materials includes high entropy alloys (HEAs). Novel MPEA compositions often have unique and superior properties compared to conventional materials. It has been shown that the features of MPEAs can be further improved by nanostructuring using severe plastic deformation (SPD) techniques. In this study, the evolution of the microstructure in MPEAs during SPD-processing (defect formation, grain refinement and phase transformation) is overviewed on the basis of the literature. The corresponding changes of the mechanical and physical properties, such as the strength, corrosion resistance and hydrogen diffusivity are discussed. In addition, the potential applications of SPD-processed MPEAs are presented. [doi:10.2320/matertrans.MT-MF2022013]

(Received January 26, 2023; Accepted February 22, 2023; Published March 17, 2023)

Keywords: *severe plastic deformation, multi-principal element alloys, high-entropy alloys, dislocations, twin faults, nanostructure, mechanical and physical properties*

1. Introduction

Presently, one of the hottest topics in materials science is the development and study of multi-principal element alloys (MPEAs).[1–3] These materials contain three or more elements with equal or near equal fractions, therefore their compositions correspond to the unexplored middle parts of the phase diagrams. The other name of these materials is complex concentrated alloys (CCAs). This new concept of alloys differs significantly from traditional solid solutions, since in MPEAs there are no solvent and solute atoms i.e., all constituents have similar roles. If the number of constituent elements in MPEAs is at least five, the high configurational entropy can stabilize the single phase structure.[4,5] These MPEAs are referred to as high-entropy alloys (HEAs).

The high interest in MPEAs is based on that (i) these novel materials may exhibit unique and never-before-seen behavior and (ii) due to the large variety of compositions different combinations of improved properties can be achieved with the help of MPEAs. For instance, MPEAs may offer a trade-off between high mechanical strength and good ductility of metallic materials.[4] This beneficial combination of mechanical properties can be achieved when face-centered cubic (fcc) and body-centered cubic (bcc) phases co-exist in MPEAs. In addition, there are MPEA compositions (e.g., NbMoTaW and VNbMoTaW) which show high strength even at elevated temperatures and these alloys are referred to as refractory MPEAs.[6] Refractory MPEAs may exhibit a higher yield strength at high temperatures (above 1000°C) than Ni-based superalloys (e.g., Inconel 718). It is worth noting that bulk metallic glasses (BMGs) are also manufactured from many principal constituents.[6] On the other hand, BMGs are brittle due to their amorphous structure, however, the crystalline MPEAs may exhibit a significant ductility beside the high strength. The underlying mechanisms behind the high strength are different for BMGs and MPEAs. Namely, for BMGs the high strength is caused by the lack of dislocations in the amorphous structure while in MPEAs the threshold stress of dislocation motion (referred to as friction stress) is enhanced due to the disordered multi-component crystalline structure.[7,8]

Coarse-grained MPEAs can be characterized by some basic features such as sluggish diffusion and severe lattice distortion.[9] These common features have a deterministic effect on the physical and mechanical behavior of MPEAs. The properties of MPEAs may deviate from the predictions made from the properties of the constituents due to the mutual interaction among these elements. This phenomenon is referred to as cocktail effect.[6,10–13] Nevertheless, the improved properties of MPEAs, such as the high strength even at elevated temperatures, the enhanced wear, oxidation, corrosion and radiation resistance, can open the door to new applications of these materials.[1,3,14–16] It is worth noting that when the number of constituents is only three or four, i.e., the MPEA is only a medium-entropy alloy (MEA) and not an HEA, the properties of materials (e.g., the hardness) can be similarly good as for higher number of composing elements.[17] Therefore, not only HEAs but also other MPEAs with three-four constituents are worth to study.

Due to the improved physical and mechanical properties of MPEAs, there are many areas of potential applications, such as hydrogen storing materials,[18,19] catalysts,[20] diffusion barriers,[21–23] cladding materials used for the nuclear fuels and high pressure vessels in nuclear power plants,[4] wear- and/or heat-resistant coatings,[4] shape memory alloys[24] and structural components.[25] In the latter case, the high mechanical strength of some MPEA compositions makes the materials suitable for advanced structural applications. The enhanced strength of MPEAs is caused by the strong resistance of the disordered crystal lattice to dislocation motion.[7,8] Very hard MPEAs were obtained when the structure of the alloys was bcc. The compressive yield strength for these materials was usually between 1000 and 2000 MPa at room temperature (RT);[26–33] however, exceptionally high yield strength of about 3500 MPa was obtained for NbMoTaWVCr HEA.[34] The latter material

*Corresponding author, E-mail: jeno.gubicza@ttk.elte.hu

was processed by mechanical alloying (MA) and subsequent consolidation by spark plasma sintering (SPS) which yielded a fine microstructure. The reduced grain size and the oxygen contamination inevitable during MA may result in an extra strengthening effect. Similar high strength was achieved for AlCrFeMoV HEA where the coexisting two bcc phases surely contributed to the outstanding mechanical performance.[34)]

The high strength of MPEAs can be further increased by applying severe plastic deformation (SPD) techniques. During SPD processing, both grain refinement and an increase of the density of lattice defects (e.g., dislocations and planar faults) contribute to hardening of the as-processed materials.[35–39)] The most frequently used SPD techniques are equal-channel angular pressing (ECAP),[40)] high-pressure torsion (HPT),[41–47)] multidirectional forging (MDF),[48)] twist extrusion (TE)[36,49)] or accumulative roll bonding (ARB).[36)] During these procedures, the bulk metallic samples are deformed up to the strains of several hundreds of percentages while their shapes do not change considerably. SPD-processing usually requires high pressure which helps to maintain the integrity of the materials by suppressing the formation and propagation of cracks. SPD can yield a grain refinement to several hundreds or tens of nanometers and an increase of the dislocation density to the order of magnitude of $10^{16}\,m^{-2}$.[37,39)] SPD-processing of MPEAs may result in a significant increase of strength and due to the grain refinement the change of the physical properties (corrosion resistance etc.) too. Therefore, it is very important to study the effect of SPD-processing on the microstructure and properties of MPEAs.

The goal of this overview is to summarize the existing knowledge on the formation of nanostructures in SPD-processed MPEAs. First, the development of the microstructure during SPD-processing is overviewed. Special emphasis is placed on the evolution of the densities of lattice defects such as dislocations and twin faults, since the multiplication, propagation and annihilation of these defects are fundamental processes during SPD and significantly influence the performance of SPD-processed materials. The characterization of the defect structure can be carried out very effectively with the non-destructive method of X-ray line profile analysis (XLPA), therefore the application specialities of this technique in the case of MPEAs are also discussed. In addition, the improvement of the mechanical and physical properties, such as strength, corrosion resistance, hydrogen diffusivity etc., due to nanostructuring and the consequent change of functionality are also overviewed.

2. Development of the Microstructure of MPEAs during SPD

2.1 Evolution of the lattice defect structure due to severe deformation

2.1.1 Fundamentals of the study of defects in MPEAs by X-ray line profile analysis

XLPA is a very effective non-destructive method for the study of lattice defects in crystalline substances. This technique is based on the fact that defects destroy the perfect atomic order in crystals, thereby resulting in broadening of the diffraction peaks.[50)] From the analysis of the peak shape, the type and density of line and planar lattice defects (e.g., dislocations and stacking or twin faults) can be determined. In addition, the average size and size distribution of crystallites can also be obtained from XLPA.[51)] This technique does not require complicated sample preparation and the statistics of the microstructural parameters obtained by this procedure is much better than that of the microscopic methods (e.g., transmission electron microscopy - TEM) due to the much larger probed volume.[50,51)] In this study, mainly XLPA is used for the determination of the density of lattice defects formed during SPD, therefore some features of this technique specific to MPEAs will be discussed in the next paragraphs.

First of all, it should be clarified how the X-ray diffraction (XRD) patterns obtained on MPEAs should be interpreted. This question arises because theoretically the peaks in an XRD pattern appear due to the periodic arrangement of atoms, while MPEAs are usually lack of strict atomic periodicity. For pure crystals, dilute alloys or highly alloyed materials with ordered structures, the periodicity is evident as shown schematically in Fig. 1(a) and (b). On the other hand, MPEAs are usually disordered solid solutions, and these structures are not strictly periodic since the lattice points are occupied by different atoms randomly (see Fig. 1(c)). Despite the disordered structure of MPEAs, their experimental XRD patterns contain peaks, similar to diffractograms of conventional alloys. In the following paragraph, this behavior is confirmed theoretically.

The intensity scattered by a crystal (I) is proportional to the product of the amplitude (A) and its complex conjugate (A^*). The amplitude can be expressed as:[50,52)]

$$A(\boldsymbol{\kappa}) \propto \sum_n F_n \exp(-2\pi i \boldsymbol{\kappa} \boldsymbol{R}_n), \tag{1}$$

where $\boldsymbol{\kappa}$ is a vector in the reciprocal space ($\kappa = 2\sin\theta/\lambda$ where θ and λ are the scattering angle and the wavelength of X-rays, respectively), $\boldsymbol{R}_n$ is the lattice vector pointing to the cell with the index n and F_n is the structure factor of the nth cell. If we consider the simplest case, when one cell contains

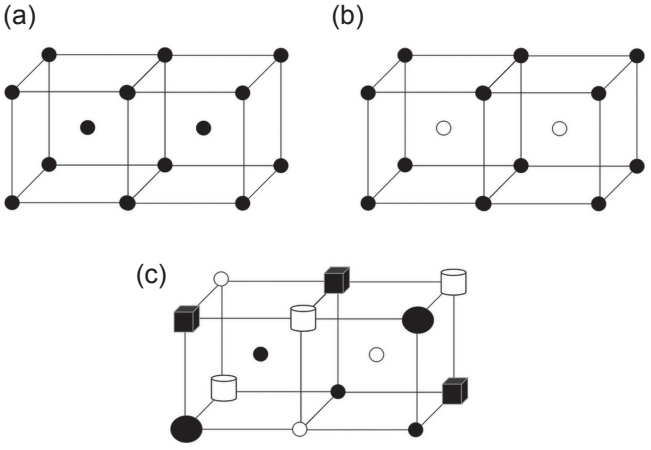

Fig. 1 Schematics showing (a) a pure crystalline structure, (b) an ordered alloy with two components and (c) a disordered MPEA structure with five constituent elements. The various atoms are indicated by different symbols.

only one atom, the structure factor of the nth cell is the same as the atomic form factor of the atom sitting in that cell (f_n). Thus, the scattered intensity is obtained as:[50,52]

$$I(\boldsymbol{\kappa}) \propto \sum_n \sum_{n'} f_n f_{n'}^* \exp[-2\pi i \boldsymbol{\kappa}(\boldsymbol{R}_n - \boldsymbol{R}_{n'})], \qquad (2)$$

where $\boldsymbol{R}_n$ and $\boldsymbol{R}_{n'}$ are the position vectors of the origins of nth and n'th cells in the lattice, respectively. Equation (2) can be rewritten as:[50,52]

$$I(\boldsymbol{\kappa}) \propto \sum_m \left(\sum_n f_n f_{n+m}^* \right) \exp(2\pi i \boldsymbol{\kappa} \Delta \boldsymbol{R}_m), \qquad (3)$$

where $\boldsymbol{\Delta R}_m = \boldsymbol{R}_{n'} - \boldsymbol{R}_n$. Since both $\boldsymbol{R}_{n'}$ and $\boldsymbol{R}_n$ are lattice vectors, $\boldsymbol{\Delta R}_m$ is also a vector connecting atomic sites. For finite crystallite size, at each value of m the summation in $\sum_n f_n f_{n+m}^*$ is carried out for those n values for which both cells with the indices n and $n+m$ are in the crystallite. Let's denote this number as N_c. If the electron density function is symmetric, i.e., $f_n(\boldsymbol{r}) = f_n(-\boldsymbol{r})$, the atomic form factor has only a real part, thus eq. (3) is simplified to the following form:

$$I(\boldsymbol{\kappa}) \propto N_c \sum_m \langle f_n f_{n+m} \rangle \exp(2\pi i \boldsymbol{\kappa} \Delta \boldsymbol{R}_m), \qquad (4)$$

where $\langle f_n f_{n+m} \rangle$ is the average of the products of the atomic form factors for all pairs of lattice sites connected by vector $\boldsymbol{\Delta R}_m$. For random distribution of elements in MPEA, $\langle f_n f_{n+m} \rangle$ is independent of $\boldsymbol{\Delta R}_m$ and equals the square of the average of the atomic form factors of the constituent elements denoted as $\langle f \rangle^2$. Thus eq. (4) can be written as:

$$I(\boldsymbol{\kappa}) \propto N_c \langle f \rangle^2 \sum_m \exp(2\pi i \boldsymbol{\kappa} \Delta \boldsymbol{R}_m). \qquad (5)$$

The last term in eq. (5), i.e., $\sum_m \exp(2\pi i \boldsymbol{\kappa} \Delta \boldsymbol{R}_m)$ give diffraction maxima when $\boldsymbol{\kappa}$ equals a reciprocal lattice vector $\boldsymbol{g}$ since the product of $\boldsymbol{g}$ and $\boldsymbol{\Delta R}_m$ is always an integer number. This condition is the same as can be obtained for traditional crystals, therefore MPEAs also must have XRD patterns decorated with diffraction peaks. According to eq. (5), the disordered structure should be considered as all atomic sites would be occupied by the same "average" atom for which the form factor equals the average of the form factors of the constituent elements weighted with their mole fractions. Thus, the structure shown in Fig. 1(c) has a bcc like diffractogram. A typical XRD pattern obtained on a bcc HfNbTiZr MPEA is shown in Fig. 2.

The peaks on the diffraction patterns of SPD-processed MPEAs are broadened due to the (i) finite crystallite size, (ii) lattice distortion caused mainly by dislocations, (iii) planar faults such as twin boundaries, (iv) instrumental broadening and (v) chemical heterogeneities which are often observed in MPEAs. These effects, if all exist, are added together by convoluting their intensity profiles, i.e.:[50,53]

$$I(\kappa) = I^i(\kappa) * f(\kappa) * I^s(\kappa) * I^d(\kappa) * I^{pf}(\kappa), \qquad (6)$$

where $*$ represents convolution, $I(\kappa)$ is the measured scattered intensity, $I^i(\kappa)$ is the instrumental peak. $I^s(\kappa)$, $I^d(\kappa)$ and $I^{pf}(\kappa)$ are the intensity profiles for the diffraction domain size, dislocations and planar faults, respectively. The chemical heterogeneities in MPEAs are taken into account by $f(\kappa)$ which is the density distribution function of the magnitude of the diffraction vector in the material.[53] The latter quantity is the reciprocal of the lattice spacing (d) which is influenced by the local chemical composition. The higher the magnitude of chemical heterogeneities, the broader the distribution of lattice spacing and also the magnitude of the diffraction vector in MPEAs. It should be noted that lattice distortion in MPEAs is caused not only by lattice defects, such as dislocations, but also the disordered alloy structure. However, the latter effect is marginal beside the XRD peak broadening caused by the high density of defects formed in SPD-processed MPEAs.

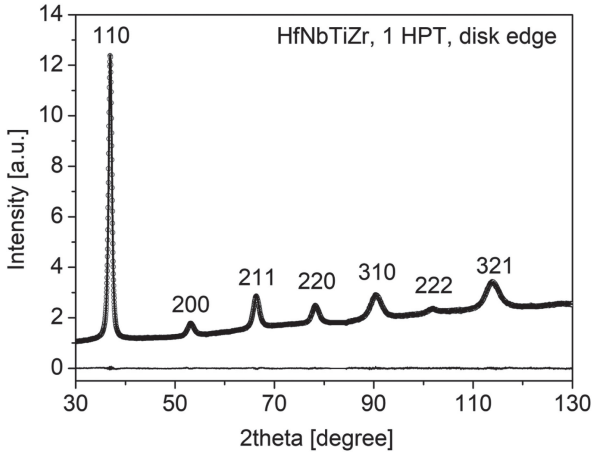

Fig. 2 XRD pattern taken on an HfNbTiZr MPEA with a bcc structure and processed by 1 turn of HPT at room temperature (RT). The diffractogram was detected at the edge of the HPT disk. The black open circles and the curve represent the measured pattern and the calculated diffractogram fitted by the CMWP method, respectively. The difference between these two patterns is shown at the bottom of the figure.

The evaluation of the shape of the diffraction peaks can be performed by fitting calculated theoretical profiles to the experimental ones. In this overview, the densities of lattice defects are determined by the convolutional multiple whole profile (CMWP) fitting method.[54] As an example, Fig. 2 illustrates a CMWP fitting on the XRD pattern taken at the edge of an HfNbTiZr MPEA disk processed by 1 turn of HPT.[55] The evaluation can yield the crystallite size, the density of dislocations and the planar fault (e.g., twin fault) probability. The latter quantity gives the fraction of faulted planes among the lattice planes lying parallel to the faults (e.g., for twin faults in fcc crystals these are the {111} planes). More details about XLPA can be found in Ref. 50). It should be noted that recently a novel machine learning based XLPA (ML-XLPA) method has been developed which opens a new way for easy and fast microstructure characterization for combinatorial MPEAs.[56] In these samples, the chemical composition varies intentionally in a wide range for studying the effect of the constituent concentrations on the phase composition and microstructure. Combining synchrotron XRD with ML-XLPA, maps of the microstructural parameters, such the defect densities, versus the chemical composition can be obtained in a very short time. In the next section, the evolution of the defect densities during SPD-processing of MPEAs is studied basically on the basis of the results obtained by XLPA technique.

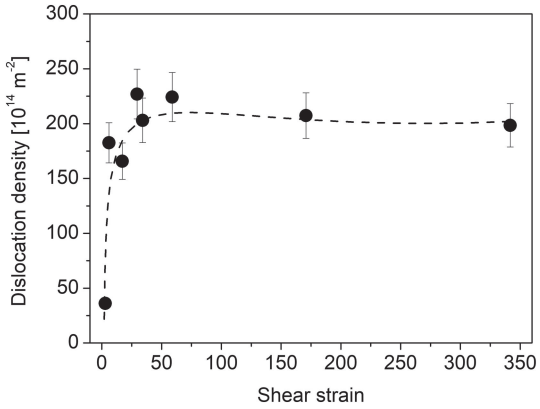

Fig. 3 The dislocation density versus the shear strain applied in HPT at RT for an HfNbTiZr MPEA. The data were taken from Ref. 55).

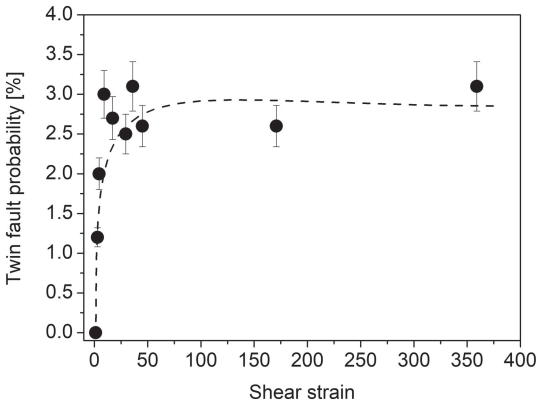

Fig. 4 The twin fault probability versus the shear strain applied in HPT at RT for a CoCrFeNi MPEA. The data were taken from Refs. 58), 59).

2.1.2 Dislocation density and twin fault probability in severely deformed MPEAs

It was found that similar to conventional alloys in MPEAs the defect density increased with increasing the strain imposed during SPD-processing. This effect is illustrated in Fig. 3 where the evolution of the dislocation density determined by XLPA versus the shear strain achieved during HPT at RT is shown for an HfNbTiZr MPEA.[55] The shear strain (γ) was determined by the following formula:

$$\gamma = \frac{2\pi r N}{t}, \tag{7}$$

where N is the number of turns, r is the distance from the disk center and t is the thickness of the disk.[24] It can be seen that the dislocation density saturated at the shear strain of 30. This value corresponds to an equivalent strain of about 17.[37] Similar threshold strain of dislocation density saturation was observed for other HPT-processed MPEAs.[53,57] The twin fault probability in fcc MPEAs with low stacking fault energy (SFE) also increases with increasing the strain imposed during SPD as illustrated in Fig. 4 for CoCrFeNi MPEA processed by HPT at RT. The data were taken from Refs. 58), 59). The saturation of twin fault probability occurred at the shear strain of ~10.

The saturation values of the dislocation density and the twin fault probability developed in different MPEAs processed by SPD at RT are listed in Table 1. These data

Table 1 The saturation values of the dislocation density and the twin fault probability developed in different MPEAs processed by SPD. HPT: High pressure torsion.

Composition	SPD method	Dislocation density [10^{14} m-2]	Twin fault probability [%]	Ref.
CoCrFeNi (fcc)	HPT at RT	156 ± 20	2.8 ± 0.4	58)
$Co_{33}Ni_{33}Cr_{19}Mn_{15}$ (fcc)	HPT at RT	280 ± 30	1.6 ± 0.2	61)
CoCrFeMnNi (fcc)	HPT at RT	194 ± 20	2.7 ± 0.2	53)
$Fe35Mn_{35}Co_{10}Cr_{10}Ni_{10}$ (fcc)	HPT at RT	236 ± 25	1.0 ± 0.1	62)
HfNbTiZr (bcc)	HPT at RT	214 ± 24	n.a.	57)
$Fe_{40}Mn_{40}Co_{10}Cr_{10}$ (hcp)	HPT at RT	71 ± 8	n.a.	62)

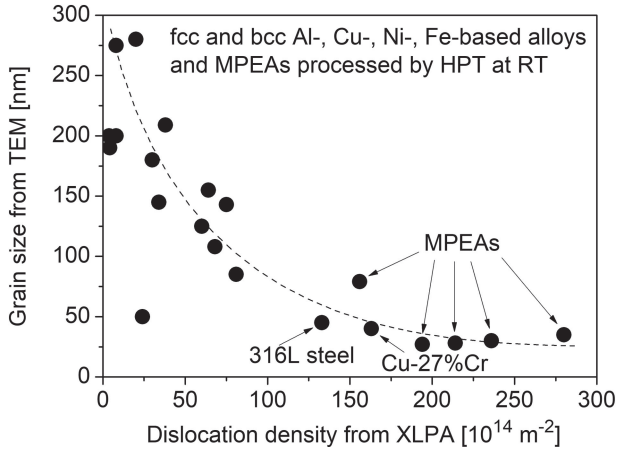

Fig. 5 The grain size determined by TEM versus the dislocation density obtained by XLPA for fcc and bcc Al-, Cu-, Ni- and Fe-based conventional alloys and MPEAs processed by HPT at RT. The plotted MPEA dislocation densities are listed in Table 1.

were obtained on samples processed by HPT since this technique is able to deform high-strength materials to very high strains (even to ~1000) while maintaining the integrity of the samples and the SPD device due to the very high applied pressure (2–10 GPa) which suppresses the initiation and propagation of cracks. The maximum dislocation density achieved by HPT at RT was about 150–280 $\times$ 10^{14} m^{-2} for the studied fcc and bcc MPEAs (see Table 1 and Refs. 57)–62)). These values are the highest among the cubic metallic alloys processed by HPT at RT as shown in Fig. 5. The high dislocation density can be explained by the retarding effect of the high melting point (~1600–2000 K for the compositions listed in Table 1) and the high degree of alloying in MPEAs on the annihilation of dislocations formed during HPT. Regarding the latter effect, in MPEAs there are high fractions of different elements with various sizes. Large atoms among the constituents of MPEAs can pin edge dislocations, thereby retarding their annihilation. It should be noted that the reduction of the temperature of HPT does not imply inevitably the increase of the dislocation density. For

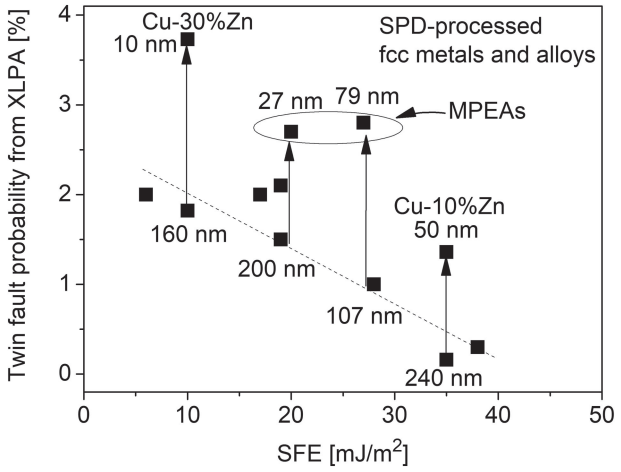

Fig. 6 Saturation twin fault probability values determined by XLPA versus the SFE for SPD-processed metals and alloys. Two MPEAs (HPT-processed CoCrFeNi and CoCrFeMnNi) are also included in the plot. The data for other materials were taken from Ref. 37). For some materials, the grain sizes are also shown, and the arrows indicate the effect of grain size on twin fault probability for the same SFEs values.

instance, in fcc $Co_{20}Cr_{26}Fe_{20}Mn_{20}Ni_{14}$ MPEA HPT-processed at LNT (77 K) the dislocation density was measured as $250 \times 10^{14}\,m^{-2}$ [63] which is in the range obtained for different MPEAs deformed by HPT at RT (see Table 1). This observation can be explained partly by fcc-to-hcp phase transformation and dynamic recrystallization during HPT at LNT, but self-annealing and static recrystallization during storage of the samples at RT after cryogenic HPT also occurred.

For MPEAs with low SFE, the large degree of dislocation dissociation also retards annihilation of dislocations, thus enhancing the saturation dislocation density.[37] In addition, a high amount of twin faults forms due to deformation twinning during SPD-processing (see Fig. 4). The saturation twin fault probability was found to be between 1 and 3%, as shown in Table 1. These values are in the same range as obtained for conventional low SFE metals and alloys, such as Ag, Cu–Al and Cu–Zn.[37] On the other hand, HPT-processed MPEAs have slightly higher twin fault probability than for conventional SPD-processed metals and alloys with the same SFE as revealed in Fig. 6. From the data listed in Table 1, only the twin fault probability values of CoCrFeNi and CoCrFeMnNi alloys are plotted in Fig. 6, since for other MPEAs SFE is not known. The SFE values were taken from Ref. 64). An enhanced twin fault probability was also observed for conventional materials in Fig. 6 which can be explained by the promoting effect of the small grain size on deformation twinning in fcc crystals. In SPD-processed MPEAs, the grain refinement is very pronounced due to the alloying effect as will be discussed in the next section, therefore a higher twin fault probability was detected than for other materials with the same SFE but higher grain size as shown in Fig. 6. It should be emphasized that the elevated twin fault probability in CoCrFeNi and CoCrFeMnNi alloys is not a specific effect for MPEAs since similar trend was also observed for conventional Cu–Zn alloys (see Fig. 6).

Although the saturation values of defect densities in different SPD-processed MPEAs have the same order of magnitude ($10^{16}\,m^{-2}$, see Table 1), the chemical composition can significantly influence the dislocation density and the twin fault probability. For instance, changing the composition from CoCrFeNi to CoCrFeMnNi with the addition of Mn increased the saturation dislocation density achievable by HPT at RT from 156 to $194 \times 10^{14}\,m^{-2}$.[58] This enhancement of the dislocation density can be attributed to three effects. First, in CoCrFeNiMn MPEA a relatively large lattice distortion develops around Mn atoms due to their larger nearest neighbor distances compared to other elements in this alloy.[65] Thus, Mn atoms can attract dislocations since the lattice distortions may be relaxed if the Mn atoms are situated in the core of dislocations. Therefore, Mn atoms in CoCrFeNiMn MPEA may have a pinning effect on dislocations, thereby hindering their annihilation during SPD-processing. Second, Mn atoms prefer the formation Mn–Co nearest-neighbor pairs at the expense of Mn–Ni pairs in CoCrFeNiMn which also impedes the motion of dislocations since the separation of Mn–Co pairs due to shear caused by dislocation glide is not favorable energetically.[66] Third, the diffusion is slower in CoCrFeNiMn than in CoCrFeNi at RT[67,68] which retards climb of edge dislocations. The above listed three effects can contribute to the development of a higher saturation dislocation density in CoCrFeNiMn HEA compared to CoCrFeNi MPEA during HPT-processing. It should be noted that the saturation twin fault probability does not differ significantly in the two alloys (2.7–2.8%) which can be attributed to the close SFEs of CoCrFeNi and CoCrFeNiMn alloys (~20–30 mJ/m^2).[64]

There may be moderate modifications of the composition of MPEAs which can yield a large difference in the maximum dislocation density achievable by HPT at RT. Table 1 shows that when Ni was added to $Fe_{40}Mn_{40}Co_{10}Cr_{10}$ and the composition became $Fe_{35}Mn_{35}Co_{10}Cr_{10}Ni_{10}$, the saturation dislocation density decreased with a factor of about 3.3. This change of the defect structure is associated with the phase transformation occurred in $Fe_{35}Mn_{35}Co_{10}Cr_{10}Ni_{10}$ during HPT.[62] Namely, the initial fcc structure transformed gradually to hcp, i.e., beside the dislocation glide transformation induced plasticity (TRIP) also contributed to deformation. Therefore, less dislocation was required for the same nominal strain of HPT than in the case of $Fe_{40}Mn_{40}Co_{10}Cr_{10}$ where the structure remained full fcc. Moreover, during fcc-to-hcp transformation the dislocations formed in the fcc phase disappeared, also contributing to the lower measured dislocation density after HPT.

Finally, it is worth noting that very high defect densities can be observed not only in SPD-processed MPEAs, but also in their nanocrystalline counterparts produced by bottom-up methods. As an example, Fig. 7 compares the defect densities of CoCrFeNi MPEA samples processed by 20 turns of HPT and physical vapor deposition (PVD).[51,69] In nanocrystalline MPEAs processed by bottom–up methods, the dislocations and twin faults are grown-in lattice defects which form in order to reduce the mismatch stresses between nanograins.

2.2 Grain refinement during SPD

As the defect density increased with increasing the imposed strain during SPD-processing, the grain size decreased and saturated at a shear strain of about 30–

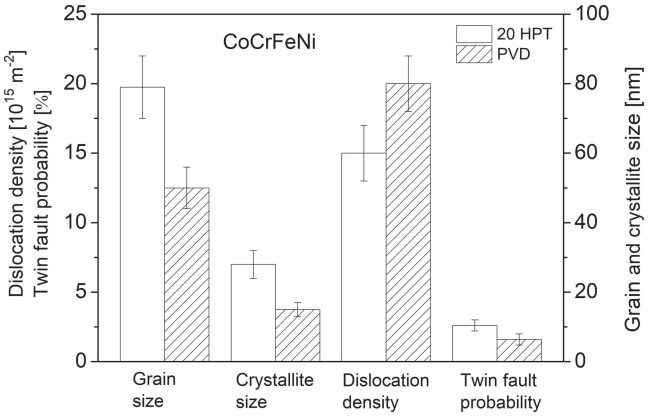

Fig. 7 Comparison of the parameters of the nanocrystalline microstructure for CoCrFeNi MPEA samples processed by 20 turns of HPT and PVD. Reproduced from Ref. 51) with the permission of the author.

40.[53,57,58)] It has been revealed that the grain refinement occurred via the following mechanisms: (i) fragmentation due to the formation of dislocation slip bands and their intersection which cause misorientations, (ii) twinning (primary and secondary) and (iii) dynamic recrystallization.[63)] The contributions of these mechanisms to grain refinement depend on the chemical composition. For instance, for compositions with low SFE, twinning has a significant role in the decrease of the grain size during SPD-processing.[53,63)] The primary twins formed in low SFE MPEAs during the early stage of SPD can be intersected with secondary twins, thereby subdividing the primary twins into equiaxed parts.[70)] In addition, the accumulation of dislocations at coherent twin boundaries yields a gradual transformation into incoherent high-angle grain boundaries (HAGBs). The grain fragmentation processes listed above also operate in conventional alloys,[37)] so they are not specific to MPEAs. In addition, fcc-to-hcp phase transformation may occur for some compositions (e.g., in $Co_{20}Cr_{26}Fe_{20}Mn_{20}Ni_{14}$ and $Fe_{40}Mn_{40}Co_{10}Cr_{10}$) during SPD-processing which can also influence the final grain size.[62,63)] These compositions usually have a low SFE since an hcp crystal can form in an fcc structure if intrinsic stacking faults develop every second {111} planes.[50)] For instance, the decrease of Ni in $(Fe,Mn)_{40-x}Co_{10}Cr_{10}Ni_x$ MPEAs resulted in an increased propensity to the development of hcp phase from fcc during HPT.[62)] Thus, during HPT at RT $Fe_{40}Mn_{40}Co_{10}Cr_{10}$ exhibited an fcc-to-hcp phase transformation while $Fe_{35}Mn_{35}Co_{10}Cr_{10}Ni_{10}$ remained fcc. The latter material has a lower saturation grain size (~30 nm) than the MPEA exhibiting phase transformation (~90 nm).[62)]

The minimum grain size achievable in MPEAs by SPD-processing are listed in Table 2. These values were determined by TEM. For all MPEAs processed by HPT at RT, the minimum grain size was lower than 100 nm, i.e., nanostructures were obtained. Considering the different MPEA compositions studied in the literature, the lowest grain size achieved by HPT in single phase MPEAs was about 30 nm (see Table 2). This value is the smallest size ever measured for metallic materials processed by HPT at RT as illustrated in Fig. 5. Slightly larger values of about 40–50 nm were obtained for highly alloyed conventional materials

Table 2 The minimum grain size achievable by SPD in MPEAs as determined by TEM. The minimum crystallite size values obtained from XLPA are also listed.

Composition	SPD method	Grain size [nm]	Crystallite size [nm]	Ref.
CoCrFeNi (fcc)	HPT at RT	79 ± 10	28 ± 3	58)
CoCrFeNi (fcc)	HPT at RT	68	n.a.	70)
$Co_{33}Ni_{33}Cr_{19}Mn_{15}$ (fcc)	HPT at RT	35 ± 5	24 ± 3	61)
CoCrFeMnNi (fcc)	HPT at RT	27 ± 5	22 ± 3	53)
CoCrFeMnNi (fcc)	HPT at RT	50	n.a.	72)
CoCrFeMnNi (fcc)	HPT at RT	33	n.a.	73)
CoCrFeMnNi (fcc)	HPT at 77 K	50	n.a.	72)
$Fe_{35}Mn_{35}Co_{10}Cr_{10}Ni_{10}$ (fcc)	HPT at RT	30 ± 5	24 ± 3	62)
$Co_{20}Cr_{26}Fe_{20}Mn_{20}Ni_{14}$ (fcc)	HPT at RT	61 ± 25	n.a.	63)
$CoCrFeMnNiTi_{0.1}$ (fcc)	HPT at RT	40	n.a.	74)
$Co_{10}Cr_{15}Fe_{35}Mn_5Ni_{25}V_{10}$ (fcc)	HPT at RT	30	n.a.	75)
HfNbTiZr (bcc)	HPT at RT	28 ± 4	17 ± 3	57)
$Fe_{40}Mn_{40}Co_{10}Cr_{10}$ (hcp)	HPT at RT	90 ± 10	19 ± 2	62)
AlCrFeCoNiNb (bcc + hexagonal Laves phase)	HPT at RT	10	n.a.	71)

such as 316L steel, Al–5.9%Mg–0.3%Sc–0.18%Zr and Cu–27%Cr alloys.[37)] It should be noted that the composition of MPEAs has a significant effect on the minimum achievable grain size as revealed by Table 2. For instance, the saturation grain size for CoCrFeNiMn HEA (~27 nm) is much smaller than that for CoCrFeNi MPEA (~79 nm) processed by HPT at RT. As discussed in section 2.1, Mn atoms have a pinning effect on lattice defects, thereby hindering the motion of grain boundaries. This effect impedes recrystallization and grain growth during SPD-processing, thus lowering the saturation grain size achieved by HPT. For MPEAs having a multiphase structure even before HPT, the minimum grain size achievable by HPT at RT can be as low as 10 nm[71)] (see also Table 2).

For most MPEAs processed by SPD, the crystallite size (or diffraction domain size) values obtained by XLPA are smaller than the grain sizes determined by TEM as shown in Table 2. This phenomenon is generally valid for not only MPEAs but all metals and alloys deformed by SPD.[37,50)] This effect can be attributed to the hierarchical nature of the SPD-processed microstructures. Namely, the grains bounded by HAGBs are fragmented into subgrains or dislocation cells whose size is measured by XLPA as the crystallite size.[50)] Indeed, the subgrain size determined by TEM agrees well with the crystallite size obtained by XLPA as demonstrated for HfNbTiZr MPEA processed by HPT in Ref. 57). In Table 2, for some compositions (e.g., for $Co_{33}Ni_{33}Cr_{19}Mn_{15}$, CoCrFeMnNi and $Fe_{35}Mn_{35}Co_{10}Cr_{10}Ni_{10}$), the grain and crystallite sizes measured by TEM and XLPA, respectively, only slightly differ, suggesting that the grains are not fragmented into subgrains after HPT-processing.

Table 3 The phases before and after SPD for MPEA compositions exhibiting phase transformation during SPD.

Composition	SPD method	Phases before SPD	Phases after SPD	Ref.
$Fe_{40}Mn_{40}Co_{10}Cr_{10}$	HPT at RT	fcc	fcc + hcp	62)
$Ti_{35}Zr_{27.5}Hf_{27.5}Nb_5Ta_5$	HPT at RT	bcc	orthorhombic	78)
$Co_{20}Cr_{26}Fe_{20}Mn_{20}Ni_{14}$	HPT at RT	fcc + σ-phase	fcc	63)
$Co_{20}Cr_{26}Fe_{20}Mn_{20}Ni_{14}$	HPT at 77 K	fcc	fcc + hcp	63)
CoCrFeMnNi	HPT at RT (10 GPa <)	fcc	fcc + bcc	72)
CoCrFeMnNi	HPT at 77 (10 GPa <)	fcc	fcc + bcc + hcp	72)
CoCrFeMnNi	Swaging at RT	fcc	fcc + hcp + amorphous	77)
AlTiFeCoNi – 0.45 wt% C	HPT at RT	ordered L21	disordered bcc	79)

2.3 Phase transformation during SPD

SPD-processing may induce phase transformation for some MPEA compositions. For instance, fcc MPEAs with low SFE, such as $Co_{20}Cr_{26}Fe_{20}Mn_{20}Ni_{14}$ and $Fe_{40}Mn_{40}Co_{10}Cr_{10}$, can transform into an hcp phase at least partly during SPD as discussed in the former section.[62,63] Table 3 lists the phases before and after SPD for those MPEA compositions which exhibited phase transformation during SPD-processing. It is worth noting that not only a decomposition of the initial single phase may occur in MPEAs but the disappearance of the secondary phase can also be observed, as shown in Table 3 (see for $Co_{20}Cr_{26}Fe_{20}Mn_{20}Ni_{14}$ processed by HPT at RT). In addition to the chemical composition of MPEAs, the conditions of SPD processing also influence the occurrence of phase transformation.[76] Namely, the method, the pressure and the temperature of SPD have an effect on phase transformation.[63,69] For instance, in the case of CoCrFeMnNi HEA the increase of the pressure of HPT above 10 GPa yielded the formation of bcc precipitates in the fcc matrix while an additional reduction of the temperature from RT to liquid nitrogen temperature (LNT, 77 K) resulted in the development of both bcc and hcp secondary phases.[69] If swaging was applied on CoCrFeMnNi HEA, SPD can yield an amorphization in the most deformed volumes beside the formation of hcp precipitates.[77]

The formation of nanosized secondary phases can lead to an additional hardening and may also influence other properties of SPD-processed MPEAs as will be shown in the next section. It should be noted, however, that the development of new phases during SPD does not imply inevitably a higher hardness. For instance, it has been shown that the elimination of Ni from $Fe_{35}Mn_{35}Co_{10}Cr_{10}Ni_{10}$ HEA (i.e., changing the composition to $Fe_{40}Mn_{40}Co_{10}Cr_{10}$) yielded fcc-to-hcp phase transformation during HPT at RT, but this phase change led to a slightly lower hardness after HPT than that for $Fe_{35}Mn_{35}Co_{10}Cr_{10}Ni_{10}$ alloy in which the structure remained fcc during HPT.[62] It was revealed that the higher hardness of the HPT-processed $Fe_{35}Mn_{35}Co_{10}Cr_{10}Ni_{10}$ MPEA was caused mainly by the higher density of lattice defects (dislocations and twin faults) since these defects formed during SPD were annihilated during phase transformation.

3. Improvement of the Properties of MPEAs due to Nanostructuring

3.1 Increase of mechanical strength

The mechanical strength of MPEAs is usually high due to the elevated friction stress caused by the disordered multiple principal element structure, as mentioned in the Introduction, and the strong solution hardening effect if the constituent elements have large differences in atomic sizes and elastic constants.[4,80] SPD-processing of MPEAs can yield additional strengthening effects caused by grain-boundaries, dislocations, planar faults (e.g., twin faults) and secondary phase precipitates.[81] For example, the application of HPT on a CoCrFeNi MPEA can almost quadruple its hardness[58] due to the refinement from a coarse-grained state (grain size: ~22 μm) to a nanocrystalline microstructure (grain size: ~80 nm), as well as enhancing the defect densities (dislocation density: $\sim 150 \times 10^{14}\,m^{-2}$, twin fault probability: ~3%). Thus, for single phase MPEAs processed by SPD the yield strength (σ_y) can be expressed by the following formula:[53]

$$\sigma_y = \sigma_0 + \alpha M^T G b \sqrt{\rho} + \frac{k}{\sqrt{d}}, \tag{8}$$

where σ_0 is the friction stress describing the crystal lattice resistance against plastic deformation, ρ is the dislocation density and d is the grain size. α is a constant describing the strengthening effect of dislocations, M^T is the Taylor factor (about 3 for untextured fcc and bcc polycrystals), G is the shear modulus, b is the modulus of the Burgers vector and k is a material constant. The values of α were 0.16 and 0.05 for HPT-processed CoCrFeMnNi and HfNbTiZr MPEAs, respectively.[53,57] The relatively low values of α can be caused by a less clustered dislocation structure due to the highly dissociated dislocation cores in both fcc CoCrFeMnNi and bcc HfNbTiZr MPEAs.[53] The values of parameter k in the Hall-Petch term were 21 and 29 $MPa \cdot \mu m^{1/2}$ for fcc CoCrFeMnNi and bcc HfNbTiZr MPEAs, respectively.[53,57] It has been shown that eq. (8) is valid for both fcc and bcc MPEAs (e.g., for CoCrFeMnNi and HfNbTiZr alloys) and in a wide range of SPD strain.[53,57] With increasing imposed strain, the fractions of the second (Taylor) term and the third (Hall-Petch) term increased. At high SPD strains, for fcc CoCrFeMnNi HEA the fractions of the friction stress, Taylor and Hall-Petch terms were about 10, 75 and 15%, respectively.[53] On the other hand, for HPT-processed bcc HfNbTiZr MPEA the largest strength contribution was given by the friction stress (about 65%) while the Taylor and Hall-Petch terms were only about 25 and 10%, respectively.[57] The much larger fraction of the friction stress in bcc MPEA compared to fcc counterparts was caused by the reduced mobility of dislocations in bcc structures. This effect is resulted by the dissociation of screw dislocation cores into a non-planar configuration which makes their motion difficult. In fcc crystals, dislocations are dissociated into partials only in their glide planes, and this planar configuration has a less pronounced retarding effect on dislocation glide. It should be

noted that for low SFE MPEAs processed by SPD the nanocrystalline grains can be subdivided into twin nano-lamellas, and the twin faults inside the grains act as obstacles against dislocation motion, similar to the general grain boundaries. Therefore, in this case the grain size (d) in eq. (8) must be substituted by the average spacing between twin faults (d_T) which can be calculated from the twin fault probability (β) determined by XLPA using the following formula:[37)]

$$d_T = 100\frac{d_{111}}{\beta}, \tag{9}$$

where d_{111} is the lattice spacing for planes $\{111\}$.

For MPEAs exhibiting phase transformation during SPD, the precipitate hardening caused by the secondary phase particles also contributes to the strength.[77,79)] The highest hardness among the reported SPD-processed MPEAs (about 10 GPa) was obtained for precipitation-hardened AlCrFeCoNiNb alloy in which the very small grain size (about 10 nm), the high dislocation density and the decomposed microstructure all contributed to the extremely high hardness.[71)] It should be noted, however, that the transformation into multiphase structure does not yield always hardening. For instance, an fcc $Fe_{40}Mn_{40}Co_{10}Cr_{10}$ MPEA underwent a martensitic transformation to hcp phase during HPT while the addition of Ni (when the composition became $Fe_{35}Mn_{35}Co_{10}Cr_{10}Ni_{10}$) stabilized the fcc structure in the SPD-processed material.[62)] The higher dislocation density in the latter composition slightly overwhelmed the hardening effect of the newly formed hcp phase in the other alloy, resulting in a slightly higher hardness for $Fe_{35}Mn_{35}Co_{10}Cr_{10}Ni_{10}$ MPEA.[62)]

With increasing the strain applied in SPD, the hardness increased and got saturated at the strain of about 40, similar to the dislocation density, twin fault probability (for low SFE MPEAs) and grain size (see section 2). This trend is illustrated for CoCrFeMnNi HEA in Fig. 8. The saturation hardness values obtained for different MPEAs are listed in Table 4. These data were plotted in Fig. 9(a) where the hardness measured after SPD processing versus the values obtained before SPD is shown. It can be seen that SPD yielded a significant enhancement of the hardness of MPEAs. The hardness increase due to SPD varies between 1400 and 4400 MPa. The ratio of the hardness values after and before SPD as a function of the initial hardness is shown in Fig. 9(b). It is revealed that a higher relative hardening can be achieved for MPEAs with lower initial hardness values. The general trend suggests that between the initial hardness values of ~1100 and ~3400 MPa the hardness ratio decreases while between ~3400 and ~6500 MPa the factor characterizing the hardness enhancement does not change significantly (its value is 1.4 ± 0.2). The inset in Fig. 9(b) shows the hardness ratio versus the initial hardness data between ~1100 and ~3400 MPa in double logarithmic scale for different MPEAs. The data points in the inset follow an approximate linear trend which suggests the following relationship:

$$\frac{H_{SPD}}{H_{init}} = A{H_{init}}^{\delta}, \tag{10}$$

where H_{SPD} and H_{init} are the hardness values after and before SPD, $A = 6870$ and $\delta = -1.05$. The almost -1 exponent is

Table 4 Hardness before deformation and maximum hardness after SPD of various MPEAs (ECAP: equal-channel angular pressing, HPT: high-pressure torsion, FSP: friction stir processing, UIT: ultrasonic impact treatment).

Composition	Before SPD [MPa]	After SPD [MPa]	Method	Ref.
CoCrNi	1570	4570	ECAP at RT	83)
CoCrFeNi	1380	5100	HPT at RT	58)
CoCrFeNi	1882	4118	ECAP at RT	84)
CoFeMnNi	1140	4290	HPT at RT	76)
$Co_{33}Ni_{33}Cr_{19}Mn_{15}$	1903	6280	HPT at RT	61)
CoCrFeMnNi	1440	5380	HPT at RT	53)
CoCrFeMnNi	1618	4766	HPT at RT	85)
CoCrFeMnNi	1570	5100	HPT at RT	86)
CoCrFeMnNi	1324	4850	HPT at RT	72)
CoCrFeMnNi	1324	5100	HPT at 77 K	72)
CoCrFeMnNi	1657	4400	shape rolling at RT	87)
CoCrCuFeNi	1470	3730	FSP at RT	88)
$CoCrFeMnNiTi_{0.1}$	1400	4500	HPT at RT	89)
$Co_{10}Cr_{15}Fe_{35}Mn_5Ni_{25}V_{10}$	2158	4953	HPT at RT	75)
$CoFeNi_2Mo_{0.2}V_{0.5}$	1570	4700	HPT at RT	90)
$CrFe_2NiMnV_{0.25}C_{0.075}$	1670	4220	HPT at RT	91)
$CrFe_2NiMnV_{0.25}C_{0.125}$	1765	4270	HPT at RT	91)
AlCoCuFeNi	3400	4850	HPT at RT	92)
$Al_{0.1}CoCrFeNi$	1320	4730	HPT at RT	93)
$Al_{0.3}CoCrFeNi$	1500	5200	HPT at RT	94)
$Al_{1.5}CoCrFeMnNi$	4590	6400	UIT at RT	95)
AlCoFeNiTi	6227	8630	HPT at RT	82)
carbon-doped AlCoFeNiTi	6200	9300	HPT at RT	79)
AlCrFeCoNiNb	6500	10100	HPT at RT	71)
AlNbTiV	6200	7400	HPT at RT	96)
$Fe_{40}Mn_{40}Co_{10}Cr_{10}$	1370	5200	HPT at RT	62)
$Fe_{35}Mn_{35}Co_{10}Cr_{10}Ni_{10}$	1290	5680	HPT at RT	62)
HfNbTiZr	2630	4330	HPT at RT	57)
HfNbTaTiZr	2940	5000	HPT at RT	97)
$Ti_{35}Zr_{27.5}Hf_{27.5}Nb_5Ta_5$	3000	3900	HPT at RT	60)

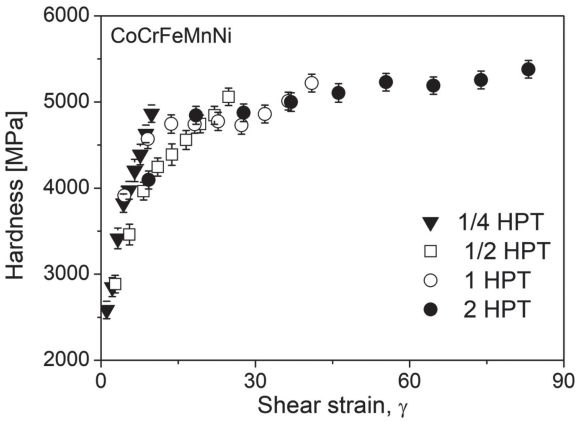

Fig. 8 The hardness versus the shear strain imposed during HPT-processing of CoCrFeMnNi HEA. The data were collected along the radius of samples processed for 1/4, 1/2, 1 and 2 turns of HPT. Reprinted from Ref. 53) with the permission of Elsevier.

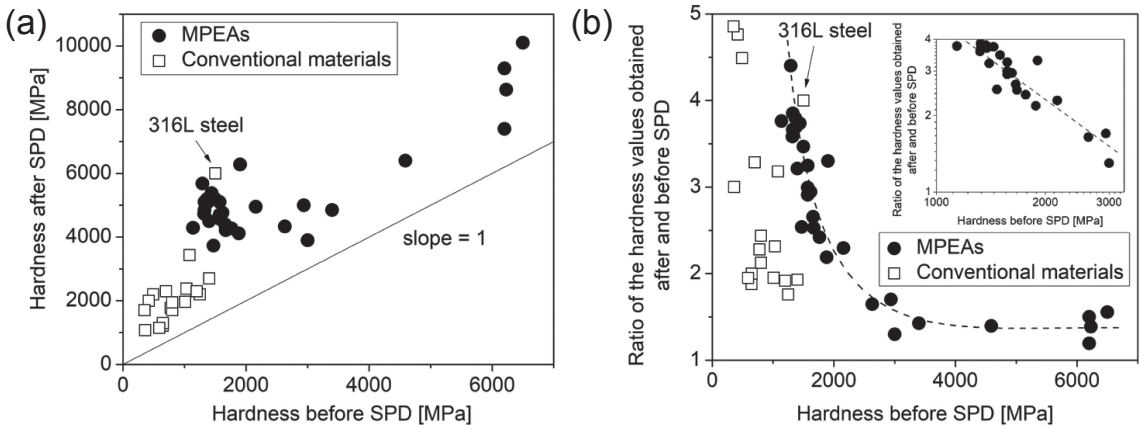

Fig. 9 (a) The maximum hardness measured after SPD-processing versus the values obtained before SPD for different conventional materials and MPEAs. The data for MPEAs were taken from Table 4. (b) The ratio of the hardness values measured after and before SPD as a function of the hardness determined before SPD for different conventional materials and MPEAs.

in accordance with the similar H_{SPD} values (5000 ± 1000 MPa) when H_{init} is between ~1100 and ~3400 MPa as shown in Fig. 9(a). It should be noted, however, that eq. (10) cannot be considered as a precise prediction of the increase of hardness since the values in Fig. 9 show significant scattering. For MPEA compositions with lower initial hardness values (between ~1100 and ~3400 MPa), the consistent maximum hardness values can be associated with the similar order of magnitude of the saturation lattice defect densities and minimum grain size which give the main contributions to the hardness after SPD. For MPEAs with very high initial hardness values (between ~6000 and ~6500 MPa), the ratio of the hardness values after and before SPD is relatively small and consistent (1.4 ± 0.2). This is due to the fact that these SPD-processed MPEAs are usually multiple-phase materials even in the initial state, and the secondary phase particles resulted in an enhanced hardness even in the initial state, therefore SPD yielded a lower relative increase of hardness.[71,79,82)] It should be noted that for any material the hardness usually increases with the reduction of the load applied in the hardness test which phenomenon is called as indentation size effect (ISE). Due to ISE, similar loads must be used if the hardness values of different materials are intended to compare. Therefore, the hardness listed in the present overview were measured with the load of about 500 g.

Figure 9 compares the hardness enhancement achieved by SPD for MPEAs and conventional metals and alloys. These conventional materials include fcc, bcc and hcp pure metals and alloys such as Ag, Cu, Nb, Ta, Al alloys, Cu alloys, Mg alloys, interstitial and stainless steels processed mainly by ECAP and HPT techniques.[98–112)] For most of these materials, the hardness values measured both before and after SPD are lower than the corresponding values of MPEAs (see Fig. 9(a)). The only exception is the 316L stainless steel processed by HPT at RT which has similar initial hardness as the lower bound for MPEAs (about 1500 MPa as shown in Fig. 9(a)), and the SPD-induced hardness increase for this material is also similar to that obtained for MPEAs with similar initial hardness. Namely, the ratio of the hardness values after and before HPT for 316L steel was about four (see Fig. 9(b)), therefore the hardness after HPT at RT increased to about 6000 MPa. Figure 9(b) shows that although conventional metals and alloys have similar hardness ratios than for MPEAs, the latter materials exhibit much higher hardness values after SPD due to the significantly higher initial hardness. The elevated initial hardness of MPEAs can be attributed to the alloying effect caused by the multi-principal element composition. Namely, segregation of some constituents may occur at the core of dislocations which retards dislocation motion. Moreover, if an energetically favorable local spatial arrangement of the components forms in an MPEA, its destruction by a shear caused by dislocation glide requires an elevated stress. In addition, for multiphase MPEAs the hard phase boundaries also contribute to the high initial hardness.

It was observed that the high strength of MPEAs caused by SPD can be further enhanced by post-deformation annealing. This phenomenon was also observed for conventional SPD-processed alloys and called as anneal-hardening.[113)] This effect was observed after annealing at moderate homologous temperatures between 0.3 and 0.4. The increases of the hardness due to annealing for different SPD-processed MPEAs are summarized in Table 5. The highest reported hardness after anneal-hardening was obtained for an AlNbTiV MPEA processed by HPT at RT and then annealed

Table 5 Maximum hardness of materials underwent hardening during post-deformation annealing.

Composition	SPD [MPa]	Annealed [MPa]	Temperature (K)	Ref.
CoCrNi	4570	5227	723	83)
CoCrFeMnNi	5100	8900	723	86)
CoCrFeMnNi	4400	5100	773	74)
$CoCrFeMnNiTi_{0.1}$	4500	5400	773	74)
$Co_{10}Cr_{15}Fe_{35}Mn_5Ni_{25}V_{10}$	4953	5266	873	75)
$CoFeNi_2Mo_{0.2}V_{0.5}$	4700	5880	873	90)
$CrFe_2NiMnV_{0.25}C_{0.125}$	4270	5440	823	91)
$Al_{0.3}CoCrFeNi$	5200	6030	773	94)
$Al_{0.5}CoCrFeMnNi$	4900	5900	1073	114)
AlNbTiV	7400	10860	973	96)
HfNbTiZr	4273	4611	740	59)

at 973 K for 15 h. Due to this treatment, the hardness increased from 7400 to 10860 MPa. Anneal-hardening can be caused by precipitation and/or phase transformation occurred during the heat treatment. For instance, sigma precipitates formed in $Al_{0.5}CoCrFeMnNi$ HEA,[114] or the single fcc phase transformed to dual fcc/bcc matrix with sigma precipitates in $CoCrFeMnNiTi_{0.1}$ alloy.[74] However, anneal-hardening can also be observed in single phase MPEAs where precipitation does not occur during heat treatment. For instance, $CoFeNi_2Mo_{0.2}V_{0.5}$ was reported to experience anneal-hardening while maintaining single fcc phase.[90] The hardening effect in this case can be attributed to the reduction of mobile dislocation density and the relaxation of grain boundary structure. In the latter process, the geometrically not necessary dislocations and excess vacancies in the grain boundaries are annihilated, therefore the boundary transforms into a more equilibrium state.[113] Due to these changes, the emission of dislocations from the grain boundaries and the grain boundary sliding become more difficult, thus plastic deformation requires a higher stress.

Figure 10(a) shows the maximum hardness obtained due to anneal-hardening for different SPD-processed MPEAs versus the hardness values measured immediately after SPD. The data were taken from Table 5. Figure 10(b) reveals that for most MPEAs the ratio of the hardness values after and before anneal-hardening is between 1.05 and 1.2, i.e., the hardness increase is maximum 20% only. There are two exceptional cases, where the hardness enhancement reached 50–75% (see also Table 5).[86,96] This very high anneal-hardening was caused by the development of nano-precipitates during heat treatment. For instance, in CoCrFeMnNi processed by HPT isochronal annealing for 1 h yielded a maximum hardness increase from 5100 to 6180 MPa when the temperature was selected as 450°C.[86] This hardening was caused by the annihilation of mobile dislocations, the grain boundary relaxation and the formation of MnNi and a Co-rich secondary phases. On the other hand, when the duration of annealing at 450°C was increased to 100 h, additional nanosized FeCo particles develop which resulted in an additional hardening to 8900 MPa.[86] In HPT-processed AlNbTiV, the exceptionally high hardness increase from 7400 to 10860 MPa during annealing at 700°C for 1 h was also caused by the development of secondary intermetallic phases Nb_2Al and Ti_3Al.[96] It is worth noting that the amount of strain in SPD-processing can significantly influence the effect of anneal-hardening. For instance, in $Al_{0.5}CoCrFeMnNi$ HEA disk processed by 5 turns of HPT anneal-hardening was observed only at the edge of the disk where (Fe,Cr)-rich σ phase developed during heat treatment at 800°C for 1 h where the very fine microstructure after HPT facilitated the new phase nucleation.[114]

3.2 Other mechanical properties: ductility, superplasticity, fatigue strength and creep resistance

The enhancement of the mechanical strength of metallic materials is usually accompanied by the reduction of ductility.[37] This general trend is also valid for MPEAs as illustrated in Fig. 11 where the ultimate tensile strength (UTS) versus the elongation to failure is plotted. In this figure, the data were obtained on SPD-processed MPEAs and also subsequently heat treated samples, and tensile testing was performed at different temperatures and strain rates. It should be noted, however, that there are special cases

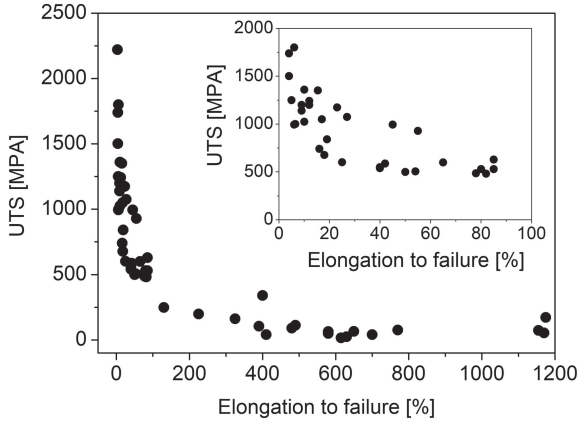

Fig. 11 The ultimate tensile strength (UTS) vs. the elongation to failure measured by tensile test at RT for different SPD-processed MPEAs. The inset shows the data related to the elongation to failure less than 100%. The data were collected from Refs. 74), 83), 115), 119)–124).

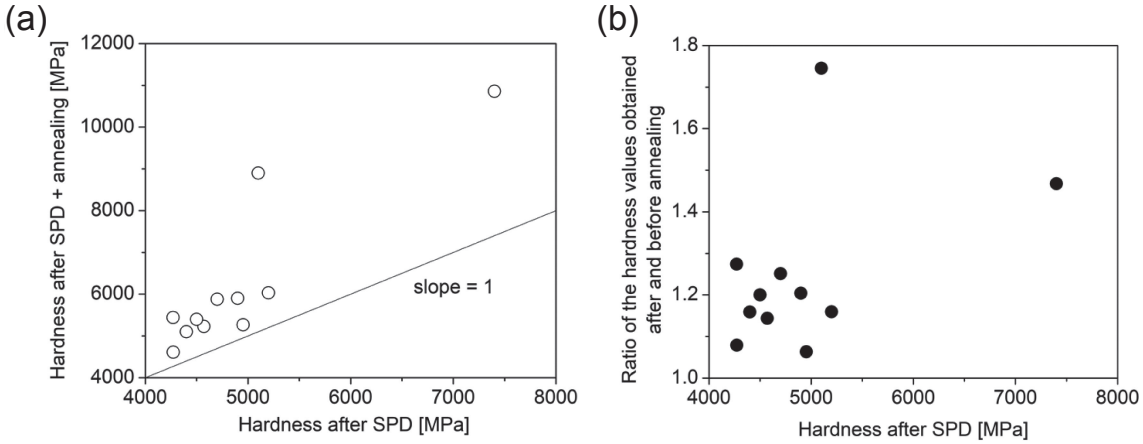

Fig. 10 (a) The maximum hardness obtained due to anneal-hardening of SPD-processed MPEAs versus the hardness values measured immediately after SPD. The data were taken from Table 5. (b) The ratio of the hardness values measured after and before anneal-hardening on SPD-processed MPEAs as a function of the hardness determined immediately after SPD.

when both the UTS and the ductility were improved via appropriate deformation and heat treatment. For instance, in the case of an $AlCoCrFeNi_{2.1}$ HEA having an UTS of 1050 MPa and an elongation to failure of 17% severe cold-rolling to 90% thickness reduction and subsequent annealing at 1273 K improved both UTS and elongation to failure to 1175 MPa and 23%, respectively.[115] This material was an eutectic mixture of ordered fcc $L1_2$ and bcc B2 phases. The same composition ($AlCoCrFeNi_{2.1}$) also showed a combination of high UTS (1360 MPa) and good elongation to failure (10%) when the as-cast material was subjected to friction stir processing.[116] From Fig. 11, it can be concluded that together with an acceptable ductility of 10–20% MPEAs can exhibit an UTS as high as 1300–1400 MPa at RT. It should be noted that similar or a better combination of strength and ductility at RT can also be achieved for other alloys which are not MPEAs. For example, Ni–5 at%Mo alloy and 316L stainless steel processed by HPT and subsequently heated up to 630 and 1000 K, respectively, exhibited UTS values as high as 1600–1700 MPa together with an elongation to failure of about 30–40%.[117,118] On the other hand refractory MPEAs (e.g., NbMoTaW and VNbMoTaW) showed a superior resistance to thermal softening due to the lower diffusion rate compared to conventional materials, such as Ni-based superalloys.[6]

In order to achieve superplasticity, which is defined as the ability to reach over 400% tensile elongation, it is crucial to apply a high testing temperature as well as the material must have a small grain size (under 10 μm).[125] The fine microstructure necessary for the occurrence of superplasticity can be achieved by SPD even for MPEAs[89,120,121,126–129] where the highest observed superplastic elongation was 2000%. This value was obtained for HPT-processed $Al_9(CoCrFeMnNi)_{91}$ at a relatively high strain rate of $5 \times 10^{-2}\,s^{-1}$.[126] While there are conventional alloys with similarly high ductility,[130] the development of MPEAs is relatively recent with very limited focus on superplasticity, leaving a lot of room for improvements. Indeed, there are reports suggesting potential properties that have influence on ductility. $Al_{0.3}CoCrNi$ appears to possess a pure Al liquid phase at the grain boundaries during high strain rate tensile test.[120] Nguyen *et al.* collected the data of several MPEAs, concluding that materials with multiple phases are more advantageous at achieving superplasticity.[121] The addition of Ti to CoCrFeMnNi reduced the grain size while increased the precipitate size, both of which improved the superplastic behavior.

In addition to strength and superplasticity, other mechanical properties of MPEAs can also be improved by SPD processing. For instance, fatigue resistance of an ultrafine-grained (UFG) CoCrFeMnNi alloy was shown to be superior to the coarse-grained (CG) counterpart during fully reversed high-cycle fatigue tests,[131] most evidently with the difference in fatigue strength (190 MPa for the CG sample and 280 MPa for the UFG sample). This superiority was explained by the more easily strain localization and cracking in CG material during fatigue. Nanocrystalline MPEAs can also be a favorable choice when developing materials with good creep resistance. The creep resistance of nanocrystalline CoCrFeMnNi was shown to be superior to nanocrystalline Ni.[73] This was explained by the creep of nanocrystalline materials at room temperature being mostly controlled by grain-boundary diffusion, which is slower in MPEAs than in conventional materials due to the sluggish diffusion nature of MPEAs.

3.3 Other properties

During SPD processing, the formation of grain boundaries, dislocations and other defects greatly increases the number of fast diffusion channels. Indeed, this can be seen in a CoCrFeMnNi HEA[132] where an HPT process can double the hydrogen diffusivity, from 1.5 to $3 \times 10^{-11}\,m^2/s$. In this case, the grain size reduction plays the dominant role in enhancing the hydrogen diffusion by promoting short-circuits diffusion. However, other defect sites such as dislocations, twin faults and vacancies can have a trapping effect, hindering the hydrogen diffusion. This was demonstrated on a cold rolled sample in which the defect density increased without grain refinement, and this change in the microstructure caused reduction of hydrogen diffusivity to $0.9 \times 10^{-11}\,m^2/s$.[132] This non-monotonic trend can also be seen in the oxidation rate of CoCrFeMnNi HEA.[133] In the first stage of deformation, when only the defect density increased, the oxidation rate was enhanced with increasing strain. On the other hand, this also induced a denser and more stable oxide layer, thereby hindering further oxidation. This results in a fast reduction of oxidation rate, and a good overall oxidation resistance. Another diffusion-driven process is corrosion, which also can be promoted or hindered by plastic deformation. Two contrast examples are CoCrFeMnNi, where cold rolling tripled the corrosion current density,[134] and $Al_{1.5}CoCrFeMnNi$, where ultrasonic impact treatment reduced the corrosion current density by over five-fold.[95]

SPD-processed MPEAs can also have a superior biocompatibility. An example is an HPT-processed TiAlFeCoNi which has a 260–1020% higher cellular metabolic activity than Ti–6%Al–7%Nb alloy or pure Ti counterparts.[82] It should be noted that for implant materials other properties such as strength, elastic modulus, toughness, wear resistance, corrosion resistance, etc., are also vital, which are also strong points of MPEAs processed by SPD as previously discussed.

4. Potential Applications of Nanostructured MPEAs Processed by SPD

Among the metallic materials, an ultra-high hardness of about 10 GPa was observed for carbon-doped AlTiFeCoNi and AlCrFeCoNiNb HEAs processed by HPT.[71,79] The outstanding hardness was attributed to the very fine grain size (about 10 nm), the high density of dislocations and the precipitates such as carbides in the case of the first alloy. For the second HEA, the dual phase microstructure consisting of cubic and hexagonal phases due to spinodal decomposition can also contribute to the very high hardness. These MPEAs with superior hardness and strength can be used in structural applications.

For MPEAs with biocompatible compositions, the improvement of mechanical performance by SPD opens the door for biomedical applications. For using as orthopedic

implants, MPEAs must fulfill the following three conditions: (i) biocompatibility, (ii) similar elastic modulus as for the human bone (about 20 GPa) and (iii) high strength. The first two conditions can be achieved by an appropriate selection of the chemical composition of the alloy. If an MPEA contains biocompatible elements, such as Ti or Mg, the implant made of this alloy does not cause inflammatory or toxic responses from the human body (i.e., there is no biological rejection). Indeed, it has been shown that equiatomic TiNbTaZrMo HEA exhibited superior biocompatibility compared to classical implant materials, such as 316L stainless steel and Ti.[135–140] It should be noted, however, that the Young's modulus of TiNbTaZrMo HEA (about 150 GPa) is larger than that of the human bone, similar to the classical implant materials.[136] The resistance against the corrosion caused by body fluids is also an important feature of surgical implants.[141]

The condition for the elastic modulus is essential for preventing osteoporosis of the human bones near the implant.[142] If the elastic modulus of the implant is much higher than the surrounding bones, the external load is bore mainly by the implant, and this load shielding effect can cause an increase of the bone porosity. It was shown that some MPEA compositions exhibit Young's moduli closer to the human bone compared to traditional biomaterials. For instance, single-phase bcc $Ti_{40}Zr_{20}Hf_{10}Nb_{20}Ta_{10}$ MPEA has similarly high strength and good ductility as for commercial hcp Ti–6%Al–4%V wrought alloy but the elastic modulus was significantly lower for this MPEA (86 GPa) compared to Ti–6%Al–4%V alloy (113 GPa).[143] In addition, the corrosion resistance and the biocompatibility of $Ti_{40}Zr_{20}Hf_{10}Nb_{20}Ta_{10}$ MPEA were remarkably better than the performance of Ti–6%Al–4%V alloy. Therefore, this MPEA composition is a potential candidate as a dental implant material. Beside surgical implants, other biomedical tools can also be made of MPEAs. For instance, $Al_{0.1}$CoCrFeNi HEA is a candidate material for peripheral vascular stent due to its high fatigue lifetime.[144] The third condition for an improved biomedical material is the high strength which can be improved by SPD in biocompatible compositions of MPEAs.[82,145] For instance, for biocompatible TiAlFeCoNi HEA HPT processing for 5 turns at RT resulted in an increase of microhardness from about 6000 to 9000 MPa.[82]

It was revealed that HPT-processed and then oxidized MPEAs are suitable materials for production of oxygen and hydrogen using photocatalytic water splitting.[146–148] Photocatalysis uses sunlight therefore the hydrogen obtained by this method can be considered as a clean fuel. The oxidation of TiZrHfNbTa HEA can result in $TiZrHfNbTaO_{11}$,[146] and additional nitriding at high temperatures can yield the formation of $TiZrHfNbTaO_6N_3$ oxynitride.[147] The pristine materials were synthesized from elemental powders using HPT. These materials exhibit a higher light absorbance and a longer operation lifetime than conventional photocatalytic substances, such as TiO_2. It is noted that both $TiZrHfNbTaO_{11}$ and $TiZrHfNbTaO_6N_3$ MPEAs are also used in photovoltaic applications when the sunlight is converted into electric current.[146,147] Additionally, these materials can be applied for photoreduction of CO_2 to CO or hydrocarbons with the help of sunlight which is an important tool in fighting against global warming.[149,150] In this process, the HPT-processed MPEAs operate as semiconductor catalyst similar to the production of hydrogen (see above). It was revealed that HPT-processed $TiZrHfNbTaO_6N_3$ MPEA exhibited a higher CO_2 photoreduction activity than the traditionally used TiO_2 ceramic material.[150] It was also found that another MPEA oxide, $TiZrNbTaWO_{12}$, has an additional advantage: this material can produce oxygen from water with the absorption of visible light while the traditional photocatalysts can work only in the ultraviolet range of sunlight.[148]

MPEAs are promising materials not only in the production but also in the storage of hydrogen fuel in a solid state form. SPD processing can improve the rates of absorption and desorption of hydrogen in MPEAs since grain boundaries, dislocations and other structural defects formed during SPD serve as path of fast diffusion. For achieving fast hydrogenation/dehydrogenation kinetics at room temperature, the composition of MPEAs is selected to fulfill the following criterion: the hydrogen binding energy should be slightly lower than 0.1 eV.[151] For instance, TiZrCrMnFeNi with a C14 Laves structure and $Ti_{0.4}Zr_{1.6}$CrMnFeNi HEA are two compositions exhibiting high hydrogenation rate, large hydrogen storage capacity and excellent cycling stability.[152,153]

It can be concluded that SPD-processed MPEAs are potential candidates for structural, biomedical and clean energy applications. In the latter field, MPEAs can be used as photocatalytic materials in reduction of CO_2 to CO or hydrocarbons, and production of oxygen or hydrogen. The storage of the hydrogen in solid state form can be performed with the help of SPD-processed MPEAs. Discovery of other important applications of this class of materials is expected in the future.

5. Summary

The evolution of the nanocrystalline microstructure in MPEAs during SPD processing was overviewed. The effect of nanostructuring on the properties (mainly on the mechanical behavior) was also discussed. Finally, the potential applications of SPD-processed MPEAs are considered. The following conclusions were obtained:

(1) During SPD processing of MPEAs at RT, the maximum density of lattice defects (e.g., dislocations and twin faults) and the minimum grain size were achieved at the equivalent strain of about 20. The maximum dislocation density and twin fault probability were about $280 \times 10^{14}\,m^{-2}$ and 3%, respectively. The minimum grain sizes for single phase and multiphase MPEAs were about 30 and 10 nm, respectively. These values are much smaller than the saturation grain sizes obtained in SPD-processed conventional metals and alloys.

(2) Due to the extremely high defect density and small grain size, the hardness of SPD-processed MPEAs is usually higher than for the conventional metals and alloys. On the other hand, the lower hardness bound of MPEAs can be achieved by conventional 316L stainless steel processed by HPT at RT. Multiphase MPEAs exhibit much higher hardness values than the single

phase counterparts. SPD-processed AlCrFeCoNiNb showed the highest hardness with the value of about 10 GPa due to the nanosized secondary phase precipitates. Anneal-hardening can further increase the mechanical strength of MPEAs. The highest hardness of about 11 GPa was achieved in AlNbTiV alloy processed by HPT at RT and then heat treated at 973 K where the anneal-hardening was caused by precipitation. Some SPD-processed MPEA compositions may exhibit excellent superplastic behavior. The highest superplastic elongation of 2000% was observed for HPT-processed $Al_9(CoCrFeMnNi)_{91}$ MPEA at 1073 K and a relatively high strain rate of $5 \times 10^{-2}\,s^{-1}$. In addition to strength and superplasticity, other mechanical properties of MPEAs, such as fatigue and creep resistance, can also be improved by SPD processing.

(3) Due to superior hardness and strength, SPD-processed MPEAs can be used in structural applications. The high strength, biocompatibility and good corrosion resistance of some MPEAs processed by SPD predestine them for surgical implant applications. In addition, there are MPEA compositions which exhibit Young's moduli closer to the human bone than in the case of traditional biomaterials. This condition is essential for preventing osteoporosis of the human bones near the implant. It was also revealed that SPD-processed and then oxidized MPEAs are suitable materials for production of oxygen and hydrogen in photocatalytic water splitting. In addition, some nanostructured MPEA compositions are promising materials in the storage of hydrogen fuel in a solid state form. In this case, SPD can improve the rates of absorption and desorption of hydrogen in MPEAs since grain boundaries, dislocations and other structural defects formed during SPD serve as path of fast diffusion. It is expected that other important applications of MPEAs will be discovered in the future. This overview revealed that from the point of view of mechanical and functional properties, the nanostructured multiphase MPEAs usually exhibited better performance than the single phase counterparts, therefore these compositions are suggested to produce and investigate in further studies.

Acknowledgments

The authors are grateful to their former partners for the cooperation in the study of SPD-processed MPEAs.

REFERENCES

1) B. Cantor, I.T.H. Chang, P. Knight and A.J.B. Vincent: Mater. Sci. Eng. A **375–377** (2004) 213–218.
2) J.-W. Yeh, S.-J. Lin, T.-S. Chin, J.-Y. Gan, S.-K. Chen, T.-T. Shun, C.-H. Tsau and S.-Y. Chou: Metall. Mater. Trans. A **35** (2004) 2533–2536.
3) J.-W. Yeh, S.-K. Chen, S.-J. Lin, J.-Y. Gan, T.-S. Chin, T.-T. Shun, C.-H. Tsau and S.-Y. Chang: Adv. Eng. Mater. **6** (2004) 299–303.
4) Y. Zhang, T.T. Zuo, Z. Tang, M.C. Gao, K.A. Dahmen, P.K. Liaw and Z.P. Lu: Prog. Mater. Sci. **61** (2014) 1–93.
5) M.-H. Tsai and J.-W. Yeh: Mater. Res. Lett. **2** (2014) 107–123.
6) O.N. Senkov, G. Wilks, J. Scott and D.B. Miracle: Intermetallics **19** (2011) 698–706.
7) Y. Wu, Y. Cai, T. Wang, J. Si, J. Zhu, Y. Wang and X. Hui: Mater. Lett. **130** (2014) 277–280.
8) G. Dirras, J. Gubicza, A. Heczel, L. Lilensten, J.-P. Couzinié, L. Perrière, I. Guillot and A. Hocini: Mater. Charact. **108** (2015) 1–7.
9) B.S. Murty, J.-W. Yeh, S. Ranganathan and P. Bhattacharjee: *High-entropy Alloys*, (Elsevier, Amsterdam, 2019).
10) S. Ranganathan: J. Curr. Sci. **85** (2003) 1404–1406.
11) S. Singh, N. Wanderka, B. Murty, U. Glatzel and J. Banhart: Acta Mater. **59** (2011) 182–190.
12) X. Wang, Y. Zhang, Y. Qiao and G. Chen: Intermetallics **15** (2007) 357–362.
13) Y. Zhou, Y. Zhang, Y. Wang and G. Chen: Appl. Phys. Lett. **90** (2007) 181904.
14) D.B. Miracle, J.D. Miller, O.N. Senkov, C. Woodward, M.D. Uchic and J. Tiley: Entropy **16** (2014) 494–525.
15) Y. Zou, H. Ma and R. Spolenak: Nat. Commun. **6** (2015) 7748.
16) O. Senkov, J. Scott, S. Senkova, F. Meisenkothen, D. Miracle and C. Woodward: J. Mater. Sci. **47** (2012) 4062–4074.
17) S. Praveen, J.W. Bae, P. Asghari-Rad, J.M. Park and H.S. Kim: Mater. Sci. Eng. A **735** (2018) 394–397.
18) Y.-F. Kao, S.-K. Chen, J.-H. Sheu, J.-T. Lin, W.-E. Lin, J.-W. Yeh, S.-J. Lin, T.-H. Liou and C.-W. Wang: Int. J. Hydrogen Energ. **35** (2010) 9046–9059.
19) I. Kunce, M. Polanski and J. Bystrzycki: Int. J. Hydrogen Energ. **38** (2013) 12180–12189.
20) C.-F. Tsai, P.-W. Wu, P. Lin, C.-G. Chao and K.-Y. Yeh: Jpn. J. Appl. Phys. **47** (2008) 5755.
21) L. Zhang, F. Wang, S. Chen and Y. Wang: Acta Metall. Sin. **49** (2013) 1611–1616.
22) M.-H. Tsai, C.-W. Wang, C.-H. Lai, J.-W. Yeh and J.-Y. Gan: Appl. Phys. Lett. **92** (2008) 052109.
23) S.-Y. Chang, M.-K. Chen and D.-S. Chen: J. Electrochem. Soc. **156** (2009) G37.
24) C. Seguí: J. Appl. Phys. **115** (2014) 113903.
25) O. Senkov, G. Wilks, D. Miracle, C. Chuang and P. Liaw: Intermetallics **18** (2010) 1758–1765.
26) Y. Cao, Y. Liu, B. Liu and W. Zhang: Intermetallics **100** (2018) 95–103.
27) A.O. Moghaddam, N.A. Shaburova, M.N. Samodurova, A. Abdollahzadeh and E.A. Trofimov: J. Mater. Sci. Technol. **77** (2021) 131–162.
28) J. Kranz, D. Herzog and C. Emmelmann: J. Laser Appl. **27** (2015) S14001.
29) N. Li, S. Huang, G. Zhang, R. Qin, W. Liu, H. Xiong, G. Shi and J. Blackburn: J. Mater. Sci. Technol. **35** (2019) 242–269.
30) H. Huang, Y. Wu, J. He, H. Wang, X. Liu, K. An, W. Wu and Z. Lu: Adv. Mater. **29** (2017) 1701678.
31) V.V. Popov, A. Katz-Demyanetz, A. Koptyug and M. Bamberger: Heliyon **5** (2019) e01188.
32) O.N. Senkov, D.B. Miracle, K.J. Chaput and J.-P. Couzinie: J. Mater. Res. **33** (2018) 3092–3128.
33) H. Zhang, Y. Zhao, S. Huang, S. Zhu, F. Wang and D. Li: Materials **12** (2019) 720.
34) F. Liu, P.K. Liaw and Y. Zhang: Metals **12** (2022) 501.
35) R.Z. Valiev, R.K. Islamgaliev and I.V. Alexandrov: Prog. Mater. Sci. **45** (2000) 103–189.
36) R.Z. Valiev, Y. Estrin, Z. Horita, T.G. Langdon, M.J. Zechetbauer and Y.T. Zhu: JOM **58**(4) (2006) 33–39.
37) J. Gubicza: *Defect Structure and Properties of Nanomaterials*, (Woodhead Publishing, Duxford, 2017).
38) R.Z. Valiev, A.P. Zhilyaev and T.G. Langdon: *Bulk Nanostructured Materials: Fundamentals and Applications*, (John Wiley & Sons, Hoboken, 2014).
39) J. Gubicza: Mater. Trans. **60** (2019) 1230–1242.
40) R.Z. Valiev and T.G. Langdon: Prog. Mater. Sci. **51** (2006) 881–981.
41) M. Kawasaki, R.B. Figueiredo, Y. Huang and T.G. Langdon: J. Mater. Sci. **49** (2014) 6586–6596.
42) A.P. Zhilyaev and T.G. Langdon: Prog. Mater. Sci. **53** (2008) 893–979.

43) K. Edalati and Z. Horita: Mater. Sci. Eng. A **652** (2016) 325–352.
44) J.-K. Han, J.-i. Jang, T.G. Langdon and M. Kawasaki: Mater. Trans. **60** (2019) 1131–1138.
45) K. Edalati: Mater. Trans. **60** (2019) 1221–1229.
46) A. Bachmaier and R. Pippan: Mater. Trans. **60** (2019) 1256–1269.
47) Z. Li, H. Ding, Y. Huang and T.G. Langdon: Adv. Eng. Mater. **24** (2022) 2200799.
48) Y. Nakao and H. Miura: Mater. Sci. Eng. A **528** (2011) 1310–1317.
49) Y. Beygelzimer, D. Orlov and V. Varyukhin: *Ultrafine Grained Materials II*, (TMS, Warrendale, PA, 2002) pp. 297–304.
50) J. Gubicza: *X-ray Line Profile Analysis in Materials Science*, (IGI-Global, Hershey, 2014).
51) J. Gubicza: Eur. Phys. J. Spec. Top. **231** (2022) 4153–4165.
52) A. Guinier: *X-ray Diffraction*, (Freeman, San Francisco and London, 1963).
53) A. Heczel, M. Kawasaki, J.L. Lábár, J.-i. Jang, T.G. Langdon and J. Gubicza: J. Alloy. Compd. **711** (2017) 143–154.
54) G. Ribárik, J. Gubicza and T. Ungár: Mater. Sci. Eng. A **387–389** (2004) 343–347.
55) P.T. Hung, M. Kawasaki, Á. Szabó, J.L. Lábár, Z. Hegedűs and J. Gubicza: Nanomaterials **12** (2022) 3371.
56) P. Nagy, B. Kaszás, I. Csabai, Z. Hegedűs, J. Michler, L. Pethö and J. Gubicza: Nanomaterials **12** (2022) 4407.
57) J. Gubicza, A. Heczel, M. Kawasaki, J.-K. Han, Y. Zhao, Y. Xue, S. Huang and J.L. Lábár: J. Alloy. Compd. **788** (2019) 318–328.
58) J. Gubicza, P.T. Hung, M. Kawasaki, J.-K. Han, Y. Zhao, Y. Xue and J.L. Lábár: Mater. Charact. **154** (2019) 304–314.
59) P.T. Hung, M. Kawasaki, J.-K. Han, J.L. Lábár and J. Gubicza: Mater. Charact. **168** (2020) 110550.
60) A. Heczel, L. Lilensten, J. Bourgon, L. Perrière, J.P. Couzine, I. Guillot, G. Dirras, Y. Huang, T.G. Langdon and J. Gubicza: Mater. Sci. Forum **879** (2016) 732–737.
61) K. Kishore, A.K. Chandan, P.T. Hung, S. Kumar, M. Kawasaki and J. Gubicza: J. Alloy. Compd. **904** (2022) 163941.
62) A.K. Chandan, K. Kishore, P.T. Hung, M. Ghosh, S.G. Chowdhury, M. Kawasaki and J. Gubicza: Int. J. Plast. **150** (2022) 103193.
63) J. Moon, Y. Qi, E. Tabachnikova, Y. Estrin, W.-M. Choi, S.-H. Joo, B.-J. Lee, A. Podolskiy, M. Tikhonovsky and H.S. Kim: Sci. Rep. **8** (2018) 1–12.
64) A. Zaddach, C. Niu, C. Koch and D. Irving: JOM **65** (2013) 1780–1789.
65) F. Zhang, Y. Tong, K. Jin, H. Bei, W.J. Weber, A. Huq, A. Lanzirotti, M. Newville, D.C. Pagan, J.Y.P. Ko and Y. Zhang: Mater. Res. Lett. **6** (2018) 450–455.
66) M. Gutierrez, G. Rodriguez, G. Bozzolo and H. Mosca: Comput. Mater. Sci. **148** (2018) 69–75.
67) M. Vaidya, S. Trubel, B. Murty, G. Wilde and S.V. Divinski: J. Alloy. Compd. **688** (2016) 994–1001.
68) M. Vaidya, K.G. Pradeep, B.S. Murty, G. Wilde and S.V. Divinski: Sci. Rep. **7** (2017) 12293.
69) P. Nagy, N. Rohbeck, Z. Hegedűs, J. Michler, L. Pethö, J.L. Lábár and J. Gubicza: Materials **14** (2021) 3357.
70) W. Wu, M. Song, S. Ni, J. Wang, Y. Liu, B. Liu and X. Liao: Sci. Rep. **7** (2017) 46720.
71) P. Edalati, A. Mohammadi, M. Ketabchi and K. Edalati: J. Alloy. Compd. **884** (2021) 161101.
72) H. Shahmir, P. Asghari-Rad, M.S. Mehranpour, F. Forghani, H.S. Kim and M. Nili-Ahmadabadi: Mater. Sci. Eng. A **807** (2021) 140875.
73) D.-H. Lee, M.-Y. Seok, Y. Zhao, I.-C. Choi, J. He, Z. Lu, J.-Y. Suh, U. Ramamurty, M. Kawasaki, T.G. Langdon and J.-i. Jang: Acta Mater. **109** (2016) 314–322.
74) H. Shahmir, M. Nili-Ahmadabadi, A. Shafiee, M. Andrzejczuk, M. Lewandowska and T.G. Langdon: Mater. Sci. Eng. A **725** (2018) 196–206.
75) P. Asghari-Rad, P. Sathiyamoorthi, N.T.-C. Nguyen, J.W. Bae, H. Shahmir and H.S. Kim: Mater. Sci. Eng. A **771** (2020) 138604.
76) F. Alijani, M. Reihanian, K. Gheisari, K. Edalati and H. Miyamoto: J. Mater. Eng. Perform. **31** (2022) 5080–5089.
77) S. Zhao, Z. Li, C. Zhu, W. Yang, Z. Zhang, D.E. Armstrong, P.S. Grant, R.O. Ritchie and M.A. Meyers: Sci. Adv. **7** (2021) eabb3108.
78) A. Heczel, Y. Huang, T.G. Langdon and J. Gubicza: Mater. Sci. Forum **885** (2017) 74–79.
79) P. Edalati, A. Mohammadi, Y. Tang, R. Floriano, M. Fuji and K. Edalati: Mater. Lett. **302** (2021) 130368.
80) D.B. Miracle and O.N. Senkov: Acta Mater. **122** (2017) 448–511.
81) G.E. Dieter and D. Bacon: *Mechanical Metallurgy*, (MacGraw-Hill, New York, 1976).
82) P. Edalati, R. Floriano, Y. Tang, A. Mohammadi, K.D. Pereira, A.D. Luchessi and K. Edalati: Mater. Sci. Eng. C **112** (2020) 110908.
83) H.W. Deng, Z.M. Xie, B.L. Zhao, Y.K. Wang, M.M. Wang, J.F. Yang, T. Zhang, Y. Xiong, X.P. Wang, Q.F. Fang and C.S. Liu: Mater. Sci. Eng. A **744** (2019) 241–246.
84) L.-M. Rymer, T. Lindner, P. Frint, M. Löbel and T. Lampke: Crystals **10** (2020) 1157.
85) D.-H. Lee, I.-C. Choi, M.-Y. Seok, J. He, Z. Lu, J.-Y. Suh, M. Kawasaki, T.G. Langdon and J.-i. Jang: J. Mater. Res. **30** (2015) 2804–2815.
86) B. Schuh, F. Mendez-Martin, B. Völker, E.P. George, H. Clemens, R. Pippan and A. Hohenwarter: Acta Mater. **96** (2015) 258–268.
87) M.S. Mehranpour, H. Shahmir and M. Nili-ahmadabadi: J. Alloy. Compd. **840** (2020) 155672.
88) N. Li, C.-L. Jia, Z.-W. Wang, L.-H. Wu, D.-R. Ni, Z.-K. Li, H.-M. Fu, P. Xue, B.-L. Xiao, Z.-Y. Ma, Y. Shao and Y.-L. Chang: Acta Metall. Sin. Engl. **33** (2020) 947–956.
89) H. Shahmir, M. Nili-Ahmadabadi, A. Shafiee and T.G. Langdon: Mater. Sci. Eng. A **718** (2018) 468–476.
90) N. Liang, R. Xu, G. Wu, X. Gao and Y. Zhao: Mater. Sci. Eng. A **848** (2022) 143399.
91) H. Shahmir, E. Tabachnikova, A. Podolskiy, M. Tikhonovsky and T.G. Langdon: J. Mater. Sci. **53** (2018) 11813–11822.
92) P. Edalati, A. Mohammadi, M. Ketabchi and K. Edalati: J. Alloy. Compd. **894** (2022) 162413.
93) P. Yu, H. Cheng, L. Zhang, H. Zhang, Q. Jing, M. Ma, P. Liaw, G. Li and R. Liu: Mater. Sci. Eng. A **655** (2016) 283–291.
94) Q. Tang, Y. Huang, Y. Huang, X. Liao, T. Langdon and P. Dai: Mater. Lett. **151** (2015) 126–129.
95) Q. Zhang, M. Li, B. Han, S. Zhang, Y. Li and C. Hu: J. Alloy. Compd. **884** (2021) 160989.
96) B. Schuh, B. Völker, V. Maier-Kiener, J. Todt, J. Li and A. Hohenwarter: Adv. Eng. Mater. **19** (2017) 1600674.
97) J. Čížek, P. Haušild, M. Cieslar, O. Melikhova, T. Vlasák, M. Janeček, R. Král, P. Harcuba, F. Lukáč, J. Zýka, J. Málek, J. Moon and H.S. Kim: J. Alloy. Compd. **768** (2018) 924–937.
98) D. Fátay, E. Bastarash, K. Nyilas, S. Dobatkin, J. Gubicza and T. Ungár: Int. J. Mater. Res. **94** (2003) 842–847.
99) P. Jenei, J. Gubicza, E. Yoon, H. Kim and J. Lábár: Compos., Part A **51** (2013) 71–79.
100) Z. Hegedűs, J. Gubicza, M. Kawasaki, N.Q. Chinh, J.L. Lábár and T.G. Langdon: J. Mater. Sci. **48** (2013) 4637–4645.
101) O. Andreau, J. Gubicza, N.X. Zhang, Y. Huang, P. Jenei and T.G. Langdon: Mater. Sci. Eng. A **615** (2014) 231–239.
102) D. Shangina, J. Gubicza, E. Dodony, N. Bochvar, P. Straumal, N.Y. Tabachkova and S. Dobatkin: J. Mater. Sci. **49** (2014) 6674–6681.
103) S. Dobatkin, J. Gubicza, D. Shangina, N. Bochvar and N. Tabachkova: Mater. Lett. **153** (2015) 5–9.
104) J. Stráská, M. Janecek, J. Gubicza, T. Krajňák, E.Y. Yoon and H.S. Kim: Mater. Sci. Eng. A **625** (2015) 98–106.
105) J. Čížek, M. Janeček, T. Krajňák, J. Stráská, P. Hruška, J. Gubicza and H.S. Kim: Acta Mater. **105** (2016) 258–272.
106) J. Gubicza, M. El-Tahawy, Y. Huang, H. Choi, H. Choe, J.L. Lábár and T.G. Langdon: Mater. Sci. Eng. A **657** (2016) 215–223.
107) G. Kapoor, T. Kvackaj, A. Heczel, J. Bidulská, R. Kociško, Z. Fogarassy, D. Simcak and J. Gubicza: Materials **13** (2020) 2241.
108) A. Khaleghi, F. Akbaripanah, M. Sabbaghian, K. Máthis, P. Minárik, J. Vesely, M. El-Tahawy and J. Gubicza: Mater. Sci. Eng. A **799** (2021) 140158.
109) J. Gubicza, M. El-Tahawy, J.L. Lábár, E.V. Bobruk, M.Y. Murashkin, R.Z. Valiev and N.Q. Chinh: J. Mater. Sci. **55** (2020) 16791–16805.
110) F. Akbaripanah, M. Sabbaghian, N. Fakhar, P. Minárik, J. Veselý, P.T. Hung, G. Kapoor, O. Renk, K. Máthis, J. Gubicza and J. Eckert: Mater. Sci. Eng. A **826** (2021) 141916.
111) B.O. Shahreza, M.A. Hernandez-Rodriguez, E. Garcia-Sanchez, L.

Kommel, F. Sergejev, A. Salinas Rodríguez, A. Heczel and J. Gubicza: Tribol. Int. **167** (2022) 107412.
112) B.O. Shahreza, J. Huot, M. Antonov, L. Kommel, F. Sergejev, F.J.P. Trujillo, A. Heczel and J. Gubicza: Int. J. Refract. Hard Met. **111** (2023) 106079.
113) J. Gubicza: Adv. Eng. Mater. **22** (2020) 1900507.
114) T. Reddy, I. Wani, T. Bhattacharjee, S. Reddy, R. Saha and P.P. Bhattacharjee: Intermetallics **91** (2017) 150–157.
115) I.S. Wani, T. Bhattacharjee, S. Sheikh, Y. Lu, S. Chatterjee, S. Guo, P.P. Bhattacharjee and N. Tsuji: IOP Conf. Ser.: Mater. Sci. Eng. **194** (2017) 012018.
116) T. Wang, M. Komarasamy, S. Shukla and R.S. Mishra: J. Alloy. Compd. **766** (2018) 312–317.
117) J. Gubicza, P.H.R. Pereira, G. Kapoor, Y. Huang, S.S. Vadlamani and T.G. Langdon: Adv. Eng. Mater. **20** (2018) 1800184.
118) M. El-Tahawy, P.H.R. Pereira, Y. Huang, H. Park, H. Choe, T.G. Langdon and J. Gubicza: Mater. Lett. **214** (2018) 240–242.
119) Y.L. Bian, Z.D. Feng, N.B. Zhang, Y.X. Li, X.F. Wang, B.B. Zhang, Y. Cai, L. Lu, S. Chen, X.H. Yao and S.N. Luo: Mater. Sci. Eng. A **847** (2022) 143221.
120) P. Asghari-Rad, N.T.-C. Nguyen, A. Zargaran, P. Sathiyamoorthi and H.S. Kim: Scr. Mater. **207** (2022) 114239.
121) N.T.-C. Nguyen, J. Moon, P. Sathiyamoorthi, P. Asghari-Rad, G.H. Kim, C.S. Lee and H.S. Kim: Mater. Sci. Eng. A **764** (2019) 138198.
122) H. Jeong and W. Kim: J. Mater. Sci. Technol. **42** (2020) 190–202.
123) S. Picak, T. Wegener, S. Sajadifar, C. Sobrero, J. Richter, H. Kim, T. Niendorf and I. Karaman: Acta Mater. **205** (2021) 116540.
124) T.A. Listyawan, H. Lee and N. Park: J. Mater. Sci. Technol. **59** (2020) 37–43.
125) M. Kawasaki and T.G. Langdon: Mater. Trans. **60** (2019) 1123–1130.
126) N.T.-C. Nguyen, P. Asghari-Rad, P. Sathiyamoorthi, A. Zargaran, C.S. Lee and H.S. Kim: Nat. Commun. **11** (2020) 2736.
127) H. Shahmir, J. He, Z. Lu, M. Kawasaki and T.G. Langdon: Mater. Sci. Eng. A **685** (2017) 342–348.
128) N.T.-C. Nguyen, P. Asghari-Rad, J.W. Bae, P. Sathiyamoorthi and H.S. Kim: Metall. Mater. Trans. A **52** (2021) 1–7.
129) N.T.-C. Nguyen, P. Asghari-Rad, A. Zargaran, E.S. Kim, P. Sathiyamoorthi and H.S. Kim: Scr. Mater. **221** (2022) 114949.
130) M. Kawasaki and T.G. Langdon: J. Mater. Sci. **42** (2007) 1782–1796.
131) Y. Tian, S. Sun, H. Lin and Z. Zhang: J. Mater. Sci. Technol. **35** (2019) 334–340.
132) J. Belo, S. Marques, A. Castilho, L. de Oliveira, R. Simao and D. dos Santos: J. Alloy. Compd. **815** (2020) 152314.
133) Y. Wang, M. Zhang, J. Jin, P. Gong and X. Wang: Corros. Sci. **163** (2020) 108285.
134) Y. Wang, J. Jin, M. Zhang, F. Liu, X. Wang, P. Gong and X. Tang: J. Alloy. Compd. **891** (2022) 161822.
135) M. Todai, T. Nagase, T. Hori, A. Matsugaki, A. Sekita and T. Nakano: Scr. Mater. **129** (2017) 65–68.
136) S.-P. Wang and J. Xu: Mater. Sci. Eng. C **73** (2017) 80–89.
137) T. Nagase, M. Todai, T. Hori and T. Nakano: J. Alloy. Compd. **753** (2018) 412–421.
138) T. Hori, T. Nagase, M. Todai, A. Matsugaki and T. Nakano: Scr. Mater. **172** (2019) 83–87.
139) Y. Yuan, Y. Wu, Z. Yang, X. Liang, Z. Lei, H. Huang, H. Wang, X. Liu, K. An, W. Wu and Z. Lu: Mater. Res. Lett. **7** (2019) 225–231.
140) A. Motallebzadeh, N.S. Peighambardoust, S. Sheikh, H. Murakami, S. Guo and D. Canadinc: Intermetallics **113** (2019) 106572.
141) R. Newell, Z. Wang, I. Arias, A. Mehta, Y. Sohn and S. Florczyk: J. Funct. Biomater. **9** (2018) 59.
142) T. Nagase, Y. Iijima, A. Matsugaki, K. Ameyama and T. Nakano: Mater. Sci. Eng. C **107** (2020) 110322.
143) S. Wang, D. Wu, H. She, M. Wu, D. Shu, A. Dong, H. Lai and B. Sun: Mater. Sci. Eng. C **113** (2020) 110959.
144) K. Alagarsamy, A. Fortier, M. Komarasamy, N. Kumar, A. Mohammad, S. Banerjee, H.-C. Han and R.S. Mishra: Cardiovasc. Eng. Technol. **7** (2016) 448–454.
145) J. González-Masís, J.M. Cubero-Sesin, A. Campos-Quirós and K. Edalati: Mater. Sci. Eng. A **825** (2021) 141869.
146) P. Edalati, Q. Wang, H. Razavi-Khosroshahi, M. Fuji, T. Ishihara and K. Edalati: J. Mater. Chem. **8** (2020) 3814–3821.
147) P. Edalati, X.-F. Shen, M. Watanabe, T. Ishihara, M. Arita, M. Fuji and K. Edalati: J. Mater. Chem. A **9** (2021) 15076–15086.
148) P. Edalati, Y. Itagoe, H. Ishihara, T. Ishihara, H. Emami, M. Arita, M. Fuji and K. Edalati: J. Photochem. Photobiol. A **433** (2022) 114167.
149) S. Akrami, P. Edalati, Y. Shundo, M. Watanabe, T. Ishihara, M. Fuji and K. Edalati: Chem. Eng. J. **449** (2022) 137800.
150) S. Akrami, Y. Murakami, M. Watanabe, T. Ishihara, M. Arita, M. Fuji and K. Edalati: Appl. Catal. B **303** (2022) 120896.
151) P. Edalati, M. Fuji and K. Edalati: arXiv preprint arXiv (2022) 2209.08291.
152) P. Edalati, R. Floriano, A. Mohammadi, Y. Li, G. Zepon, H.-W. Li and K. Edalati: Scr. Mater. **178** (2020) 387–390.
153) A. Mohammadi, Y. Ikeda, P. Edalati, M. Mito, B. Grabowski, H.-W. Li and K. Edalati: Acta Mater. **236** (2022) 118117.